Geophysical Journal International

Geophys. J. Int. (2017) **210,** 774–786
Advance Access publication 2017 May 5
GJI Seismology

doi: 10.1093/gji/ggx190

Lowermost mantle anisotropy near the eastern edge of the Pacific LLSVP: constraints from SKS–SKKS splitting intensity measurements

Jie Deng,[1] Maureen D. Long,[1] Neala Creasy,[1] Lara Wagner,[2] Susan Beck,[3] George Zandt,[2] Hernando Tavera[4] and Estela Minaya[5]

[1]*Department of Geology and Geophysics, Yale University, New Haven, CT* 06520*, USA. E-mail: jie.deng@yale.edu*
[2]*Department of Terrestrial Magnetism, Carnegie Institution for Science, Washington, DC* 20012*, USA*
[3]*Department of Geosciences, University of Arizona, Tucson, AZ* 85721*, USA*
[4]*Instituto Geofisico del Peru, Lima, Peru*
[5]*San Calixto Observatory, Bolivia*

Accepted 2017 May 4. Received 2017 April 20; in original form 2016 December 27

SUMMARY

Seismic anisotropy has been documented in many portions of the lowermost mantle, with particularly strong anisotropy thought to be present along the edges of large low shear velocity provinces (LLSVPs). The region surrounding the Pacific LLSVP, however, has not yet been studied extensively in terms of its anisotropic structure. In this study, we use seismic data from southern Peru, northern Bolivia and Easter Island to probe lowermost mantle anisotropy beneath the eastern Pacific Ocean, mostly relying on data from the Peru Lithosphere and Slab Experiment and Central Andean Uplift and Geodynamics of High Topography experiments. Differential shear wave splitting measurements from phases that have similar ray paths in the upper mantle but different ray paths in the lowermost mantle, such as SKS and SKKS, are used to constrain anisotropy in D″. We measured splitting for 215 same station-event SKS–SKKS pairs that sample the eastern Pacific LLSVP at the base of the mantle. We used measurements of splitting intensity(SI), a measure of the amount of energy on the transverse component, to objectively and quantitatively analyse any discrepancies between SKS and SKKS phases. While the overall splitting signal is dominated by the upper-mantle anisotropy, a minority of SKS–SKKS pairs (∼10 per cent) exhibit strongly discrepant splitting between the phases (i.e. the waveforms require a difference in SI of at least 0.4), indicating a likely contribution from lowermost mantle anisotropy. In order to enhance lower mantle signals, we also stacked waveforms within individual subregions and applied a waveform differencing technique to isolate the signal from the lowermost mantle. Our stacking procedure yields evidence for substantial splitting due to lowermost mantle anisotropy only for a specific region that likely straddles the edge of Pacific LLSVP. Our observations are consistent with the localization of deformation and anisotropy near the eastern boundary of the Pacific LLSVP, similar to previous observations for the African LLSVP.

Key words: Pacific Ocean; Seismic anisotropy; Kinematics of crustal and mantle deformation.

1 INTRODUCTION

The D″ layer is the lowermost ∼200–300 km of the mantle above the core–mantle boundary. It is characterized by both lateral seismic velocity heterogeneity and significant seismic anisotropy, in contrast to the bulk of the overlying lower mantle, and likely plays an important role in mantle dynamics (e.g. Garnero *et al.* 2004; Lay & Garnero 2004). Seismic waveform studies suggest a sharp vertical seismic discontinuity at the top of D″ (Sidorin *et al.* 1999) and a phase transformation from bridgmanite to post-perovskite (Murakami *et al.* 2004) is often invoked to account for this discontinuity. Seismic tomography models suggest the presence of two broad regions with relatively lower shear wave speeds and higher than average density centred beneath the Pacific and Africa (Trampert *et al.* 2004), known as large low shear velocity provinces (LLSVPs). A smaller region of reduced shear velocities beneath Eurasia, known as the Perm Anomaly, may represent a smaller structure with similar thermochemical properties (Lekic *et al.* 2012).

Localized patches where *S*-wave velocity is reduced up to ∼30 per cent, known as ultra-low-velocity zones (ULVZs), have been observed near the edge of and within the LLSVPs (e.g. Rost *et al.* 2005; Lay *et al.* 2006; McNamara *et al.* 2010). Lowermost mantle structures such as LLSVPs and ULVZs are related to fundamental questions about deep-mantle convection, core–mantle interaction and the thermal and chemical evolution of the earth (e.g. Garnero *et al.* 2016).

In contrast to the overlying lower mantle, which is generally considered to be (nearly) seismically isotropic (e.g. Meade *et al.* 1995; Panning & Romanowicz 2006), D″ generally exhibits strong anisotropy (e.g. Wookey & Kendall 2007; Nowacki *et al.* 2011). Many observations of anisotropy in D″ are consistent with vertical transverse isotropy, a specific geometry of anisotropy in which $V_{SH} > V_{SV}$ (e.g. Lay & Helmberger 1983; Wookey & Kendall 2007). However, there are some regions in D″ where more complex styles of anisotropy are inferred, including tilted transverse isotropy and azimuthal anisotropy (e.g. Wookey & Kendall 2007; Nowacki *et al.* 2011). Constraints on D″ anisotropy mostly arise from examining shear waves with nearly horizontal propagation directions through D″ (e.g. S, ScS or S_{diff}). These phases have long ray paths in D″, but usually have limited azimuthal distribution, and only sample anisotropy in a horizontal ray path geometry. However, SKS and SKKS phases travel through the lowermost mantle at a different propagation direction (∼30°–55° from vertical), and are theoretically sensitive to azimuthal anisotropy in D″ (Wookey & Kendall 2007). Moreover, the ray paths of SKS and SKKS from the same event/station pair are similar in the upper mantle and deviate significantly only in the lowermost mantle. Discrepant SKS–SKKS splitting is therefore potentially very useful to investigate lowermost mantle anisotropy.

Global studies of SKS–SKKS differential splitting show that only ∼5 per cent of cases present pronounced SKS–SKKS splitting discrepancies due to anisotropy in the lowermost mantle (Niu & Perez 2004; Restivo & Helffrich 2006). Contributions to SK(K)S splitting from lowermost mantle are thus not a first-order global effect; however, several regional studies have documented discrepant SKS–SKKS splitting and shed important light on the structure and dynamics of the lowermost mantle (Long 2009; He & Long 2011; Vanacore & Niu 2011).

A particularly interesting recent observation is the presence of lowermost mantle anisotropy near the edges of both the African LLSVP (Wang & Wen 2007; Cottaar & Romanowicz 2013; Lynner & Long 2014; Ford *et al.* 2015; Long & Lynner 2015) and the Perm Anomaly (Long & Lynner 2015). Observations suggest that there is strong lowermost mantle anisotropy at the edge of the African LLSVP, but weak, absent, or complex anisotropy within its boundaries. Those observations, along with the documented presence of lowermost mantle anisotropy proximal to the Perm Anomaly, may indicate particularly strong lowermost mantle deformation at the borders of low shear velocity provinces (LSVPs). This inferred deformation along LSVP margins might produce crystallographic- or shape-preferred orientation and consequently make the lowermost mantle seismically anisotropic.

This lowermost mantle deformation scenario proposed for the African LLSVP and the Perm Anomaly could possibly also apply to the Pacific LLSVP. However, so far no study has been carried out to examine the anisotropic structure of the eastern portion of the Pacific LLSVP due to the paucity of seismic data. Thanks to recent temporary deployments in western South America, specifically the Peru Lithosphere and Slab Experiment (PULSE) and Central Andean Uplift and Geodynamics of High Topography (CAUGHT) projects, we now have sufficient seismic records that sample the eastern edge of Pacific LLSVP at the base of the mantle. In this study, we combine data from the PULSE and CAUGHT arrays with data from seven permanent stations in southern Peru, northern Bolivia and Easter Island to probe lowermost mantle anisotropy beneath the eastern Pacific. We investigated the splitting of SKS and SKKS phases to identify possible discrepant splitting due to lowermost mantle anisotropy, with the goal of testing the hypothesis that anisotropy is concentrated at the edge of the Pacific LLSVP, as observed beneath Africa.

2 SPLITTING ANALYSIS: METHODS AND RESULTS

2.1 Station and event distribution

We identified high-quality seismograms with clear SKS and SKKS arrivals using data from 91 broad-band seismic stations of the PULSE and CAUGHT networks as well as seven permanent stations (NNA, LPAZ, AP01, GO01, GO02, RPN and VA04) (Fig. 1). A sketch of the ray paths of an SKS–SKKS pair for the same event

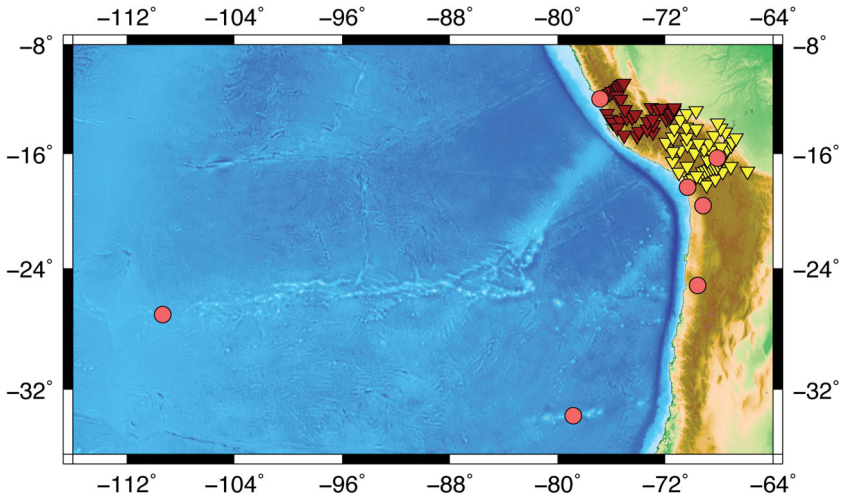

Figure 1. Map of stations used in this study, from the PULSE network (red triangles), CAUGHT network (yellow triangles) and seven permanent stations (NNA, LPAZ, AP01, GO01, GO02, RPN and VA04; pink circles).

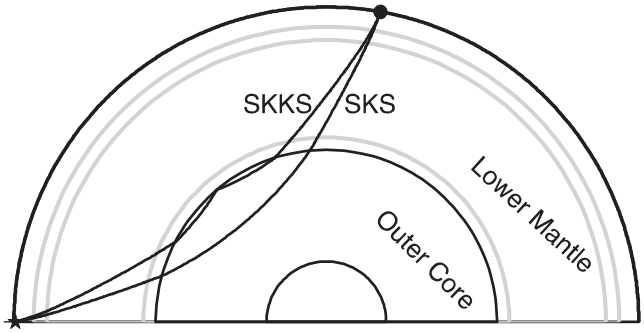

Figure 2. Sketch of SKS and SKKS ray paths for a source (star)—receiver (solid circle) epicentral distance of 115°. Grey lines indicate major mantle discontinuities. Note the similar sampling of the upper mantle—and different sampling of the lowermost mantle—for SKS and SKKS phases.

and station, illustrating their similar sampling of the upper mantle but their different sampling of the lowermost mantle, is shown in Fig. 2. We selected events of magnitude $M_w \geq 5.8$ at epicentral distances between 108° and 140° for analysis (Fig. 3). All waveforms were bandpass filtered to retain the energy at periods between 8 (or 10) and 25 s, with the lower period bound chosen manually to optimize signal-to-noise ratio (SNR) and waveform clarity for each individual waveform.

2.2 Shear wave splitting methodology

We used the SplitLab software package (Wüstefeld *et al.* 2008) to simultaneously apply the rotation correlation and transverse component minimization measurement methods to measure the splitting parameters (fast direction, φ and delay time, δt). We only retained splitting measurements with high SNR and good waveform clarity, and for which the splitting parameters estimated by the two methods agreed within the 2σ formal errors (typically $\pm 25°$ for the fast direction and ± 0.7 s for delay time). In addition to this estimation of the splitting parameters (φ, δt), we also modified the SplitLab code to calculate the splitting intensity (SI) following the method described by Chevrot (2000). SI is defined as the amplitude of the transverse component, $T(t)$, relative to the time derivative of the radial component, $R'(t)$. We measured the SI by projecting the transverse component onto the time derivative of the radial component, which yields an optimal estimate of SI for noisy data (Chevrot 2000):

$$\mathrm{SI} = -2\frac{T(t)R'(t)}{\|R'(t)\|^2}, \tag{1}$$

where $\|R'(t)\|^2$ is the squared norm of $R'(t)$. The definition of mean square error from appendix B in Chevrot (2000) is used to estimate the 95 per cent confidence of each SI measurement. For the simple case of a homogeneous layer of anisotropy, the apparent shear wave splitting parameters (ϕ, δt) can be related to the transverse and radial component energy via the equation

$$T(t) \approx -\frac{1}{2}(\delta t \sin 2\beta)R'(t), \tag{2}$$

where β is the angle between the fast direction (ϕ) and the incoming polarization direction of the wave (equivalent to the backazimuth for SK(K)S phases). Therefore, SI is approximately related to the apparent splitting parameters by

$$\mathrm{SI} \approx -\frac{1}{2}\delta \mathrm{t} \sin 2\,\beta. \tag{3}$$

We define null arrivals as those that exhibit nearly linear uncorrected particle motion, as well as an absolute splitting intensity value, abs(SI), less than 0.2. An example of splitting measurements for a same station-event SKS–SKKS pair, along with the measured SI values, is shown in Fig. 4.

2.3 Shear wave splitting results

We identified 215 well-characterized SKS–SKKS pairs. Of these, 82 consisted of pairs that exhibited consistent splitting parameters, while 133 exhibited at least some difference in estimated splitting parameters (i.e. they exhibited a difference in measured SI when the error bars were taken into account). The geographic distribution of the lowermost mantle sampling for our data set is shown in Fig. 5, and a table containing our individual measurements can be found in Table S1in the Supporting Information.

We categorized most of the 215 SKS–SKKS pairs into four regional groups based on the positions of their pierce points relative to the geographical pattern of Pacific LLSVP edge, as inferred from the GyPSuM tomography model of Simmons *et al.* (2010, Fig. 5). SK(K)S phases of Regions I and II are configured such that

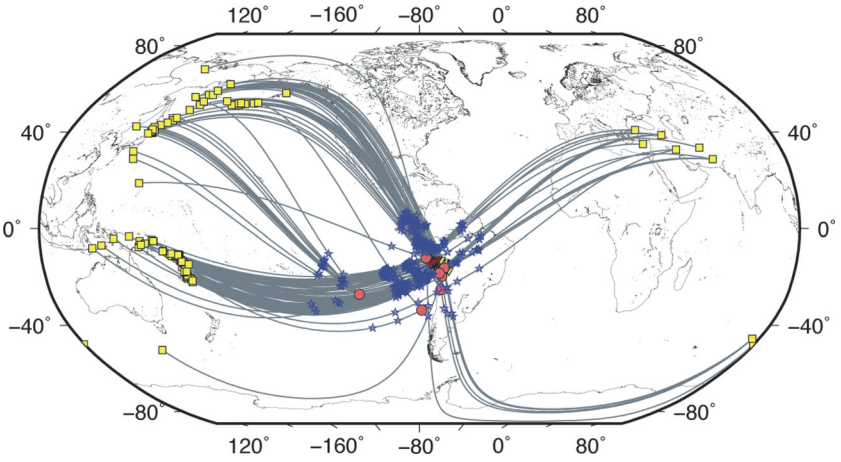

Figure 3. Locations for all earthquakes that yielded at least one usable SKS–SKKS splitting pair. Grey lines denote great circle paths for the pairs, along with the surface projection (blue stars) of the receiver-side 2700 km depth pierce point for SKS and SKKS. Pierce points are calculated using TauP toolkit based on IASP91 earth model (Crotwell *et al.* 1999).

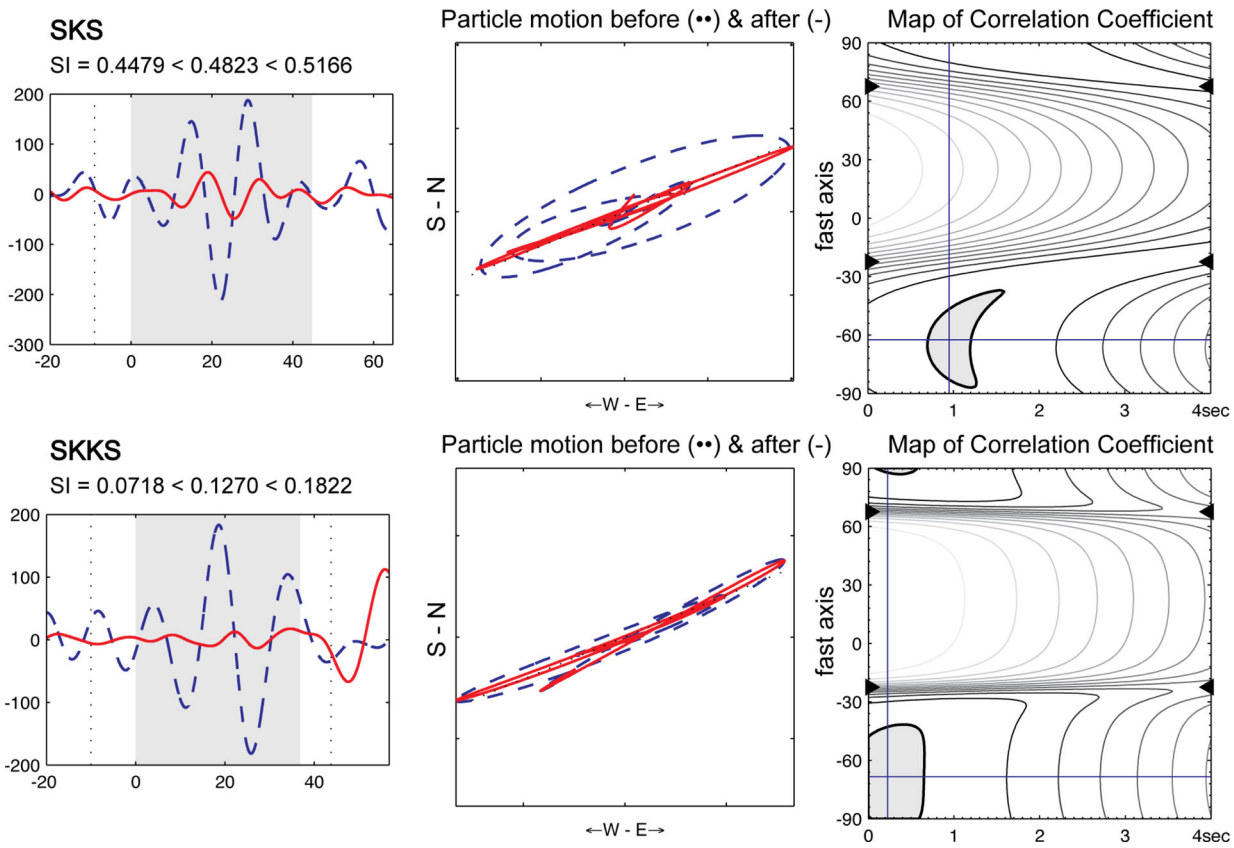

Figure 4. A representative SKS–SKKS splitting measurement. We show measurements using the rotation-correlation method and splitting intensity methods at station CB42 for an event on 2012 January 9 ($M_w = 6.4$, backazimuth = 248°, depth = 33 km and $\Delta = 121°$). Columns show the radial (dashed) and transverse (solid) components of the phase (left-hand panels), the initial (dashed) and corrected (solid) particle motion (centre panels) and the map of the correlation coefficient for all possible (φ, δt) pairs (right-hand panels), with the best-fitting parameters marked with the crossed lines. Top row: the SKS phase exhibits pronounced transverse energy, elliptical uncorrected particle motion, and clear evidence of splitting: well-constrained splitting parameters of $\varphi = -62°$ and $\delta t = 1$ s are obtained. The corresponding SI of the SKS phase is $0.4479 < 0.4823 < 0.5166$. Top row: The SKKS phase exhibits little transverse energy, linear particle motion, and null or near-null splitting. The corresponding SI of SKS phase is $0.0718 < 0.1270 < 0.1822$.

SKKS pierce points sample within the negative shear wave velocity anomaly, while SKS pierce points (partially) fall into positive shear wave velocity. While Regions I and II are adjacent to each other, they sample slightly different regions (with Region II rays sampling just to the east of Region I rays) and are associated with slightly different ray propagation azimuths in our data set (Fig. 5). Pierce points of SK(K)S phases of Region III sample within the region of relatively low shear velocities, and thus within the body of the LLSVP, while those in Region IV sample the region outside the LLSVP. We note that Region III is only sampled by data recorded at one station, RPN, and that rays sampling this region propagate over a range of azimuths.

3 DISCRIMINATING THE LOWER MANTLE CONTRIBUTION

3.1 Strong upper-mantle contributions

Most of stations in this study are located in the northern part of the Central Andean Plateau or the southern portion of Peru, which has been shown by several previous studies to exhibit strong and complex anisotropy in the upper mantle associated with subduction-related deformation (Eakin *et al.* 2014, 2015; Antonijevic *et al.* 2016; Long *et al.* 2016). Therefore, we expect that our set of SK(K)S measurements primarily reflects upper-mantle anisotropy beneath the corresponding stations, with only a subtle contribution, if any, from the lowermost mantle. In order to evaluate the contribution from the upper mantle, we plotted all our SK(K)S splitting measurements at the station locations (Fig. 6) and compared our measured splitting parameters with previous studies of the upper-mantle anisotropy for the same region. The SK(K)S arrivals at stations in northern Central Andean Plateau (NNA, AP01, GO01, GO02, LPAZ, PULSE and CAUGHT networks) generally exhibit trench-parallel fast directions and ∼1 s delay times, with some geographic variability, in a good agreement with the previous studies about the upper-mantle anisotropy in the same region (Eakin & Long 2013; Eakin *et al.* 2015; Long *et al.* 2016). Splitting results at RPN are consistent with previous results (e.g. Wolfe & Silver 1998), primarily reflecting the oceanic upper-mantle anisotropy. Overall, the consistency between our splitting measurements and previous upper-mantle anisotropy studies (based on both shear wave splitting and on surface wave phase velocities) at the same stations suggests a strong upper-mantle contribution to the shear wave splitting in this study. Despite this, we can examine our data set for evidence of discrepant splitting between SKS and SKKS arrivals for the same event-station pairs that might suggest a contribution from the lowermost mantle.

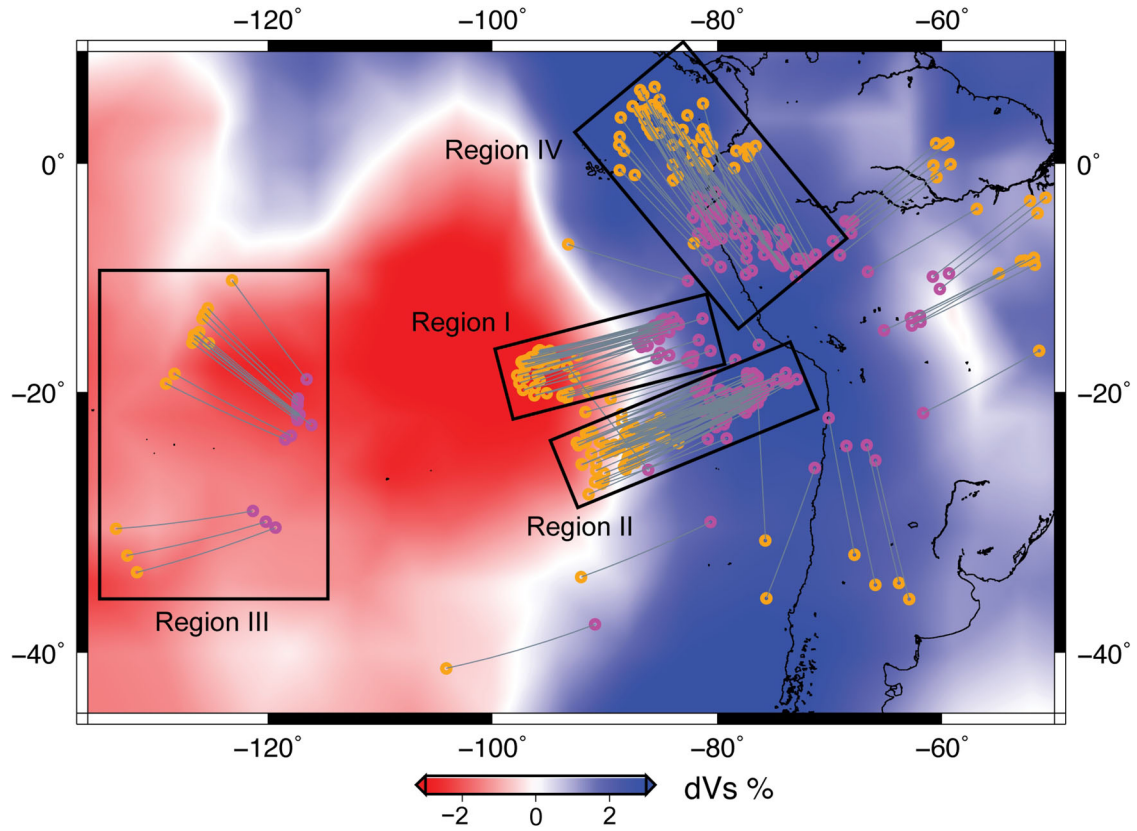

Figure 5. Geographic coverage of our data set. We plot pierce points of the 215 SKS–SKKS pairs in our data set at a depth of 2700 km, near the base of the mantle. Magenta circles show pierce points for SKS phases, while orange circles represent SKKS pierce points. Background colours show *S*-wave velocity perturbations for the GyPSuM tomography model (Simmons *et al.* 2010) at a depth of 2700 km. SKS–SKKS pairs are categorized into four regional groups (area constrained by boxes) based on the positions of their pierce points relative to lowermost mantle features.

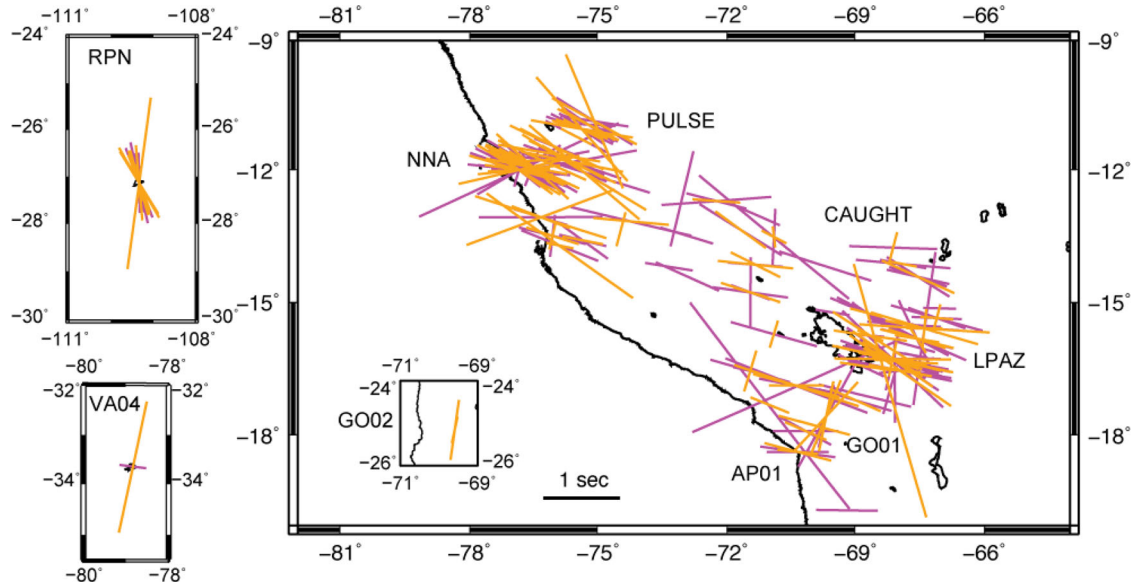

Figure 6. Non-null SK(K)S splitting results plotted at stations. Each splitting measurement is represented by a bar (yellow denotes the SKKS phase and magenta denotes the SKS phase), oriented by φ and scaled in length by δt. Scale bar at the bottom of map represents 1 s delay time.

3.2 Sks–skks splitting intensity discrepancies and their interpretation

The upper mantle beneath the CAUGHT and PULSE arrays is characterized by complex and multilayered anisotropy; this impedes explicit corrections for upper-mantle anisotropy, as has been implemented in some previous studies of lowermost mantle anisotropy using SKS–SKKS (e.g. Lynner & Long 2014; Long & Lynner 2015). Instead, we investigate the SI values measured for our data set and evaluate discrepancies between the SKS and SKKS phases. In general, pronounced differences in shear wave splitting (as expressed

in SI values) between the phases suggest a contribution from lowermost mantle anisotropy to one or both phases (e.g. Niu & Perez 2004); however, we must first rule out heterogeneous upper-mantle anisotropy or full waveform effects as making major contributions to the observed discrepancies. Previous work taking into account finite frequency wave propagation (for homogeneous upper-mantle anisotropy models) has shown that modest differences in SI (up to ~ 0.2) for SKS and SKKS phases of the same event-station pair can result from waveform interference effects (Lin *et al.* 2014). Specifically, Lin *et al.* (2014) showed that waveform interference can strongly affect SKS–SKKS SI measurements for shallow sources (<20 km) at epicentral distances less than than ~100°. In the epicentral distance range, we use in this study (108°–140°), we expect waveform interference in the upper mantle to alter the SIs of the same station-event SKS–SKKS pairs by at most 10 per cent, with maximum interference at distances of ~130° (*Lin et al.* 2014). (One important but subtle point is that Lin *et al.* (2014) used a slightly different formulization for SI than that of Chevrot (2000), which is the formulation we use in our work; these formulations are different by a factor of 0.5). Based on these arguments, we exclude waveform interference as the primary cause of SKS–SKKS SI discrepancies greater than ~0.2. Ideally, it should be possible to group SKS–SKKS measurements by epicentral distance to identify any systematic patterns as an additional check; while this has been done for other SKS–SKKS splitting discrepancy studies (e.g. Long & Lynner 2015), for our data set it is very difficult to separate the potential effects of epicentral distance and regional heterogeneity.

A second question is to what extent lateral variations in upper-mantle anisotropy over short length scales may contribute to discrepant SKS–SKKS splitting. In order to evaluate this possibility, we computed pierce points at 200 km depth in the upper mantle for SKS and SKKS phases for the maximum epicentral distance used in this study (140°). At this distance, the SKS and SKKS pierce points are separated by only ~11 km at a depth of 200 km. Thus, an explanation for SKS–SKKS discrepancies that invokes upper-mantle heterogeneity as a primary cause would require variability on this very short length scale. Upper-mantle anisotropy has been extensively studied beneath the PULSE and CAUGHT arrays, using both shear wave splitting (Eakin *et al.* 2014, 2015; Long *et al.* 2016) and surface wave tomography (Antonijevic *et al.* 2016). These studies found that while anisotropy patterns do vary laterally, the variations are generally inferred to be over considerably longer length scales (particularly for SKS splitting). We argue, therefore, that pronounced discrepancies in SI between SKS and the corresponding SKKS phase (greater than roughly 0.4, to allow for some modest contribution from upper-mantle structure) generally require some contribution from anisotropy in the lowermost mantle (see also discussions in Lynner & Long 2012). SKS–SKKS pairs with subtle differences in measured SI, in contrast, may reflect full waveform effects or small-scale heterogeneity in upper-mantle anisotropy.

Keeping these arguments in mind, we construct a series of map views of our SI discrepancy measurements (Fig. 7) that invoke a series of threshold differences between the SI values for the pairs of phases, and use these maps to infer likely contributions from lowermost mantle anisotropy. We define the minimum SI discrepancy (ΔSI) as the absolute difference between the lower bound of the larger SI and upper bound of smaller SI for a same station-event SKS–SKKS pair (i.e. we take into account the error bars on the SI estimates when we evaluate the differences between SKS–SKKS pairs). The maps in Fig. 7 should be interpreted keeping in mind

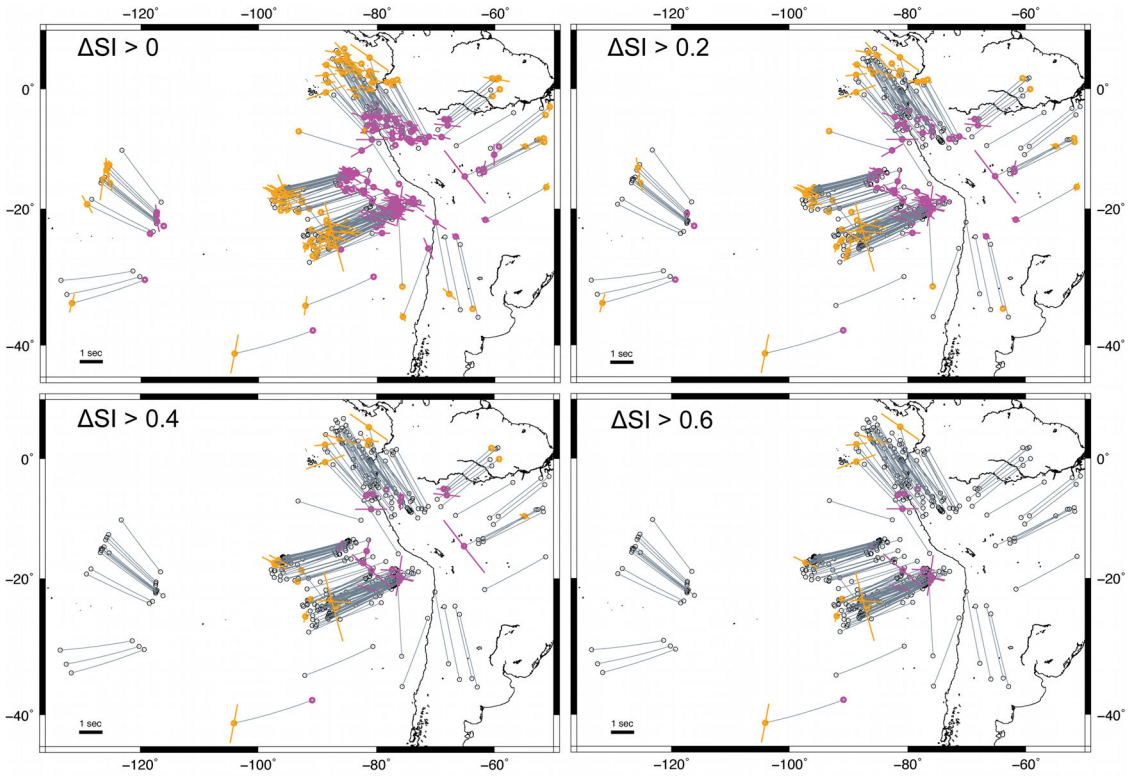

Figure 7. 215 SKS/SKKS pairs plotted at 2700 km pierce points. Red and orange circles are SKS and SKKS phase from discrepant pairs. All non-discrepant pairs are shown in white circles. The orientation and length of magenta (SKS) and orange (SKS) bars correspond to measured fast directions and delay times, respectively. ΔSI is defined as the absolute difference of lower bound of the larger SI and upper bound of smaller SI for a same station-event SKS–SKKS pair. The minimum ΔSI is set as 0, 0.2, 0.4 and 0.6 as shown in each panel.

that the larger the difference in SI for any given pair, the higher the likelihood of a contribution to splitting (to one or both phases) from lowermost mantle anisotropy. Again, this argument hinges on the fact that SKS and SKKS phases for the same event-station pair have very similar ray paths in the upper mantle and crust (Fig. 2).

As expected, the number of non-discrepant pairs in our data set increases with the increase of the SI discrepancy threshold (Fig. 7). For a threshold ΔSI value of 0.4, we observe no discrepant pairs in Region III, whereas Regions I, II and IV exhibit a mixture of discrepant and non-discrepant pairs. The lack of discrepant pairs sampling within Region III suggests that there is no pronounced lowermost mantle contribution to splitting in this region. For other regions, the lower mantle is likely to contribute to the observations, but the extent and nature of this contribution is unclear from simple visual inspection of Fig. 7 due to the complex nature of the splitting pattern, with a mixture of discrepant and non-discrepant pairs observed. This mix of splitting behaviour is typical in SKS–SKKS splitting discrepancy studies (e.g. Long 2009; Lynner & Long 2014; Long & Lynner 2015), although the scatter is particularly pronounced for our eastern Pacific study region. The scatter in individual SKS–SKKS discrepancy measurements, which likely reflects a combination of small-scale variations in anisotropic structure and natural variability in noisy seismic data, suggests the need to consider stacking approaches, which we discuss below.

3.3 A stacking approach: methods and results

In order to extract robust and quantitative constraints on the contribution to splitting from lower mantle anisotropy in different regions, we developed a stacking approach to enhance possible lower mantle signals. This approach involved the alignment and stacking of radial and transverse component waveforms within individual regions, in order to enhance the signal and identify robust differences between the SKS and SKKS transverse component waveforms. We implemented direct stacking of SKS and SKKS waveforms separately (we refer to this as stacking method no. 1) as well as a differencing approach (stacking method no. 2) in which we directly subtracted SKS and SKKS waveforms and measured the SI of the stacked and differenced transverse component waveforms, as described below. Our stacking approach relies upon the fact that the SI is a commutative quantity (Chevrot 2000; Silver & Long 2011) and the contribution of successive layers of anisotropy to transverse component waveforms (and thus SI) can, at least in principle, simply be summed (Chevrot 2000). Conversely, phases that have undergone the same splitting due to upper-mantle anisotropy but different splitting due to lowermost mantle anisotropy can be differenced to identify the (differential) contribution from the lowermost mantle. This property of SI (and thus the transverse component waveforms) contrasts with the non-commutative behaviour of the traditional splitting parameters ϕ and δt (Silver & Long 2011).

For direct stacking (stacking method no. 1), we followed the cross-correlation method described by Shearer (1991) to align the radial component seismograms; the same time delays were used to align and stack the transverse component seismograms. Within each region, we identified a ∼40 s window wavelet centred on the maximum amplitude point on a single seismogram to use as a reference waveform. The cross-correlation functions between this wavelet and the rest of the seismograms in the same region were computed, and appropriate time-shifts were found by identifying the maximum absolute values of cross-correlation functions. We manually checked the polarities of each seismogram in order to avoid cycle skipping, and in a few cases we flipped the polarities to maintain similarity with the reference arrival. We then applied the same time-shift and polarity change for the transverse component. To illustrate our approach, we show in Fig. 8, the aligned normalized radial, radial derivative and transverse components of SKS and SKKS phases in Region III after time-shift and polarity reversal. While the reference radial waveforms are not identical, they are very similar; this similarity of the radial component waveforms within each region helps to demonstrate the validity of a stacking approach for SK(K)S data. We note that the transverse component waveforms in Fig. 8 reflect both contributions from the (complexand heterogeneous) upper-mantle anisotropy beneath the stations as well as a (potential) contribution from the lowermost mantle; therefore, it is unsurprising that we observe a great deal of variability among the individual transverse components.

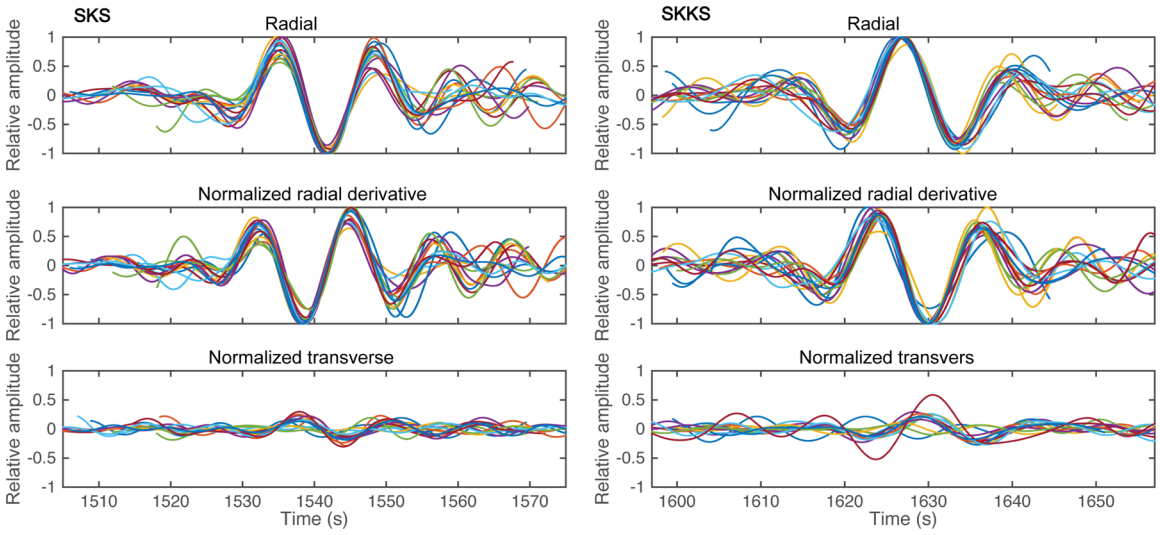

Figure 8. Aligned and normalized SK(K)S waveforms for region III. The components from the same station-event pairs are shown in the same colour. The radial component waveforms are extremely similar for each phase; as expected, however, the transverse components are different, reflecting different upper-mantle anisotropy contributions over different azimuths at the same station (RPN). For other regions, we stack over a single azimuth but over a set of stations with variable upper-mantle anisotropy contributions to splitting.

Table 1. Summary of splitting measurements for SK(K)S same station-event pairs from four regions. Measured SI values are shown with 95 per cent confidence regions in the square brackets.

Region	Number of pairs	Stacked SKS	Stacked SKKS	Stacked SKS–SKKS	Ratio of SKS–SKKS with abs(SI) < 0.4 (per cent)
I	15	0.3957 [0.3623 0.4291]	0.1038 [0.0823 0.1252]	0.2453 [0.2204 0.2703]	67
II	58	0.3213 [0.2985 0.3441]	0.2849 [0.2610 0.3089]	0.0242 [0.0104 0.0380]	76
III	15	0.26 [0.2280 0.2920]	0.3666 [0.3240 0.4093]	−0.0262 [−0.0437 −0.0087]	87
IV	54	−0.3266 [−0.3372 −0. 3160]	−0.3343 [−0.3450 −0.3235]	0.0304 [0.0198 0.0410]	85

After cross-correlation and alignment, the radial and transverse component seismograms of SK(K)S phases were summed, producing stacked waveforms (stacking method no. 1). The SIs of the stacked seismograms for each phase type (SKS and SKKS) for each of our four selected geographic regions, along with error estimates based on the 95 per cent confidence limits, were measured from the stacked seismograms and are shown in Table 1. Because the SI values for the stacked waveforms reflect both a contribution from upper-mantle anisotropy (which should be similar for both phase types) and a potential lowermost mantle contribution, any difference can be attributed to the lowermost mantle. Only Region I exhibits an SI discrepancy between the stacked SKS and SKKS waveforms that is statistically different than zero (∼0.40 for SKS versus ∼0.10 for SKKS; the error estimates suggest that a difference of at least ∼0.24 is required by the waveforms). In contrast, the ΔSI values measured from the stacked SK(K)S phases in Regions II and IV are very close to zero. The measured ΔSI for Region III is slightly larger, but cannot be distinguished from zero given the relatively large uncertainties on the measured SI values for the stacked SKS and SKKS waveforms (Table 1).

As an alternative (but in theory equivalent) approach, we also stacked the residual waveforms of the same station-event SKS and SKKS pairs for each region; that is, for each SKS–SKKS pair we subtracted the transverse component seismograms for each phase to obtain a differenced transverse component (stacking method no. 2). These differenced waveforms were then stacked within regions and SI was measured for the stacked and differenced transverse components (Fig. 9). For each SKS–SKKS pair, SKS and SKKS arrivals were aligned via cross-correlation as described above, using the radial component of SKS phase as the reference. The time derivatives of the radial component of SK(K)S were also aligned and normalized by scaling each amplitude to one. The time derivatives of radial component of SKS and SKKS were averaged to obtain a new (stacked) radial component waveform for this SKS–SKKS pair. Transverse components of the SKS and SKKS arrivals were aligned and normalized by the scaling factors that applied to the corresponding radial component derivative. The residual waveform of the transverse component for this SKS–SKKS pair was then computed by directly subtracting these two waveforms. Applying the same procedure to each SKS–SKKS pair yields a corresponding residual waveform, including a new time derivatives of radial component and a new transverse component. We then once again stacked and normalized the residual waveforms in each region, as shown Fig. 9. Only the stacked residual transverse component waveform for Region I exhibits a pronounced amplitude on the transverse component (with error bars on the SI estimate that argue that it is statistically significant; Table 1), indicating a likely differential contribution to splitting from the lowermost mantle. Indeed, the consistency of the stacked waveforms, which were measured at many different stations, provides an additional argument that upper-mantle anisotropy cannot explain the observed SKS–SKKS discrepancies; if the discrepant splitting of individual SKS–SKKS pairs were due to upper-mantle anisotropy that varied over short length scales, one would not expect the consistent stacked signals over the relatively large geographic region.

We calculated the SI values for the differenced transverse component waveforms obtained via stacking method no. 2 and plotted them as histograms (Fig. 10). The mean values of the SIs of residual waveforms (red line) and the SIs of the stacked residual waveforms (blue line) are also shown for comparison. The similarity of these two values for all four regions is a result of the commutative property of the SI, and indicates that our interpretation is not affected by which stacking method is used. The distribution of measured SI values for SKS resembles that for SKKS in most regions with the exception of Region I, as demonstrated in Fig. 10. As a result, only in Region I do the SIs of the residual waveforms (SKS–SKKS) centre around a value other than zero. Although the histograms shown in Fig. 10 (reflecting ΔSI values for individual pairs of differenced waveforms) are fairly broad for each of the four regions, the calculated 95 per cent confidence intervals on the stacked and differenced SI estimates (Table 1) demonstrate that the non-zero SI measurement on the stacked and differenced waveform for Region I is statistically significant.

We now consider a comparison between Fig. 7, which shows Regions I, II and IV are all characterized by at least some discrepant pairs at a threshold ΔSI value up to 0.6, and Figs 9 and 10, which demonstrate that only Region I has substantial, statistically significant non-zero SI discrepancies for stacked and differenced waveforms. The scatter and complexity in the individual SKS–SKKS discrepancy measurements in Fig. 7 is likely due in large part to noise; individual SKS–SKKS SI measurements are more sensitive to noise, while the stacked SI measurements should be less so. Therefore, for this particular data set, we view the stacked results as more robust than the individual results. We point out that this data set exhibits substantially weaker SKS–SKKS discrepancies, and more scattered individual measurements, than many published SKS–SKKS data sets (e.g. Long *et al.* 2009; Lynner & Long 2014). Indeed, this aspect of our observations prompted us to develop the stacking methods that we present here; for other published data sets, the observed discrepancies and their interpretation are more clear-cut from individual SKS–SKKS measurements. Thus, our results do not change the interpretation of previously published SKS–SKKS discrepancy studies; however, the stacking method we develop here could potentially be a powerful tool for discriminating subtle

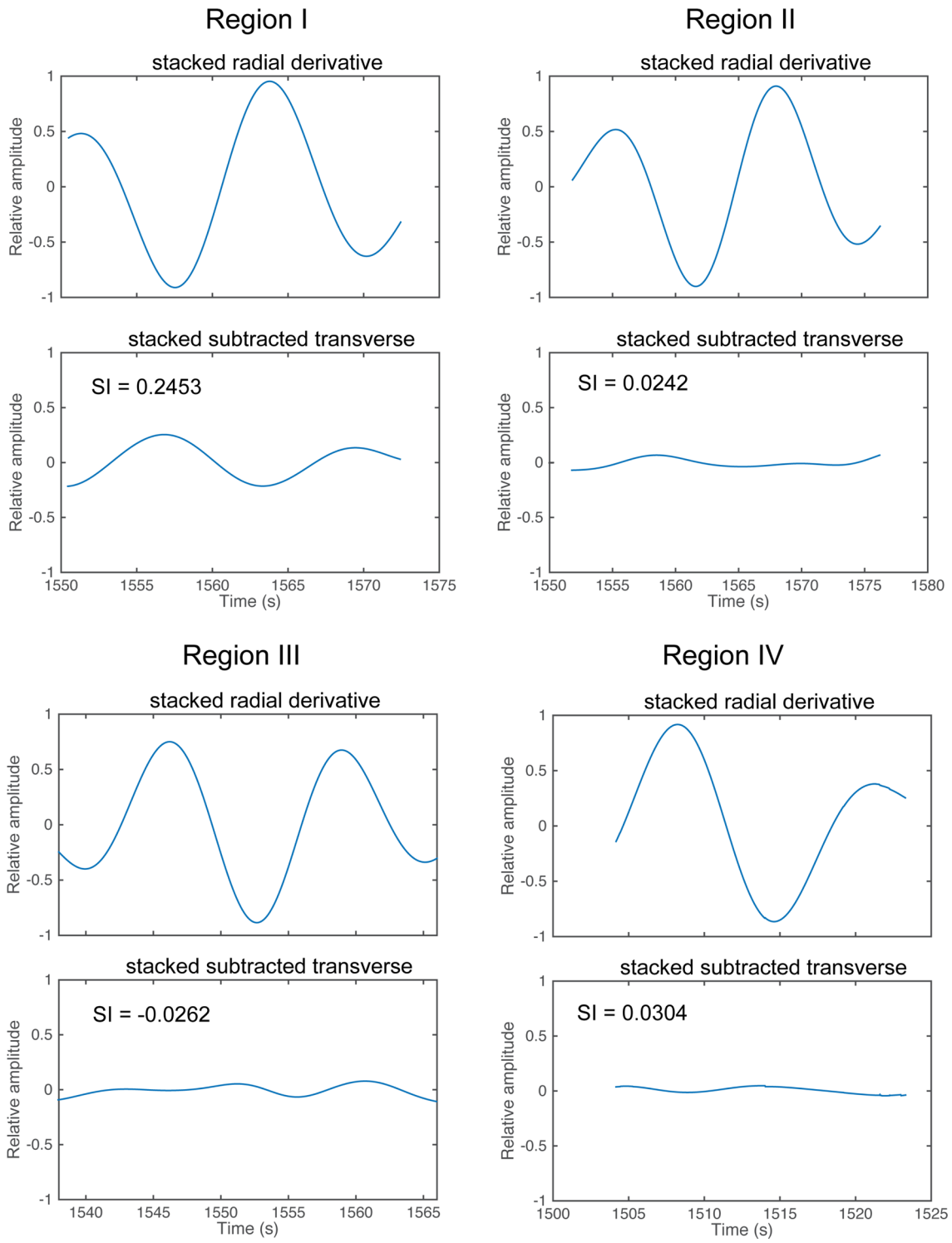

Figure 9. Normalized stacked time derivatives of radial component and stacked subtracted transverse component for four regions. The amplitude of transverse component is amplified by a factor of 2 for clarity and to emphasize the waveform shape. Note that the shape of the transverse component waveform for Region I has the same shape as the radial component derivative, as predicted by theory (Chevrot 2000).

SKS–SKKS discrepancies that may not be large enough to reliably detect using individual SKS–SKKS pairs.

To summarize our observations and inferences, two different stacking procedures yield the same result that only the splitting of waveforms sampling Region I exhibits a pronounced and statistically significant lower mantle anisotropy contribution. More specifically, the stacked Region I waveforms indicate that the SK(K)S phases sampling this region are experiencing a contribution to SI from lowermost mantle anisotropy that is different for SKS and SKKS phases. Because our two different stacking methods yield generally consistent results, this gives us additional confidence that the stacking approach is in fact robust for real data. However, our data set cannot rule out the possibility that lower mantle anisotropy exists in the other three regions, as splitting due to lowermost

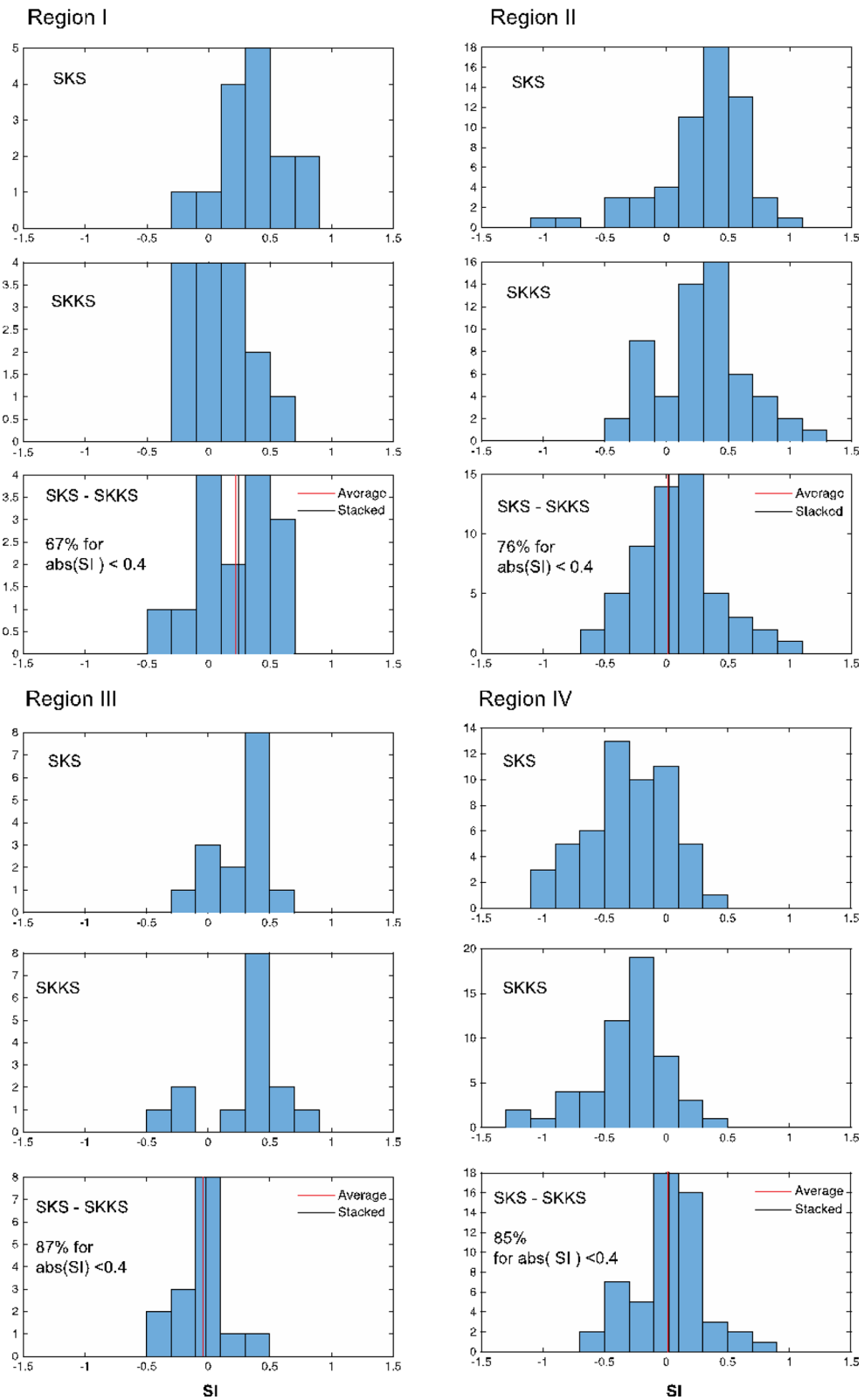

Figure 10. Histograms of SI values for SKS and SKKS phases and residual (differenced) waveforms (SKS–SKKS) for each region. Red line represents the mean value of the SIs of residual waveforms. (Recall that for each region, differenced transverse component waveforms are computed for every SKS–SKKS pair, and the SI of each residual waveform is calculated.) Blue line represents the SI of the stacked differenced waveforms. (Again, recall that within each region, the differenced transverse waveforms for all the SKS–SKKS pairs are stacked and the SI of the resultant stacked waveform is calculated).

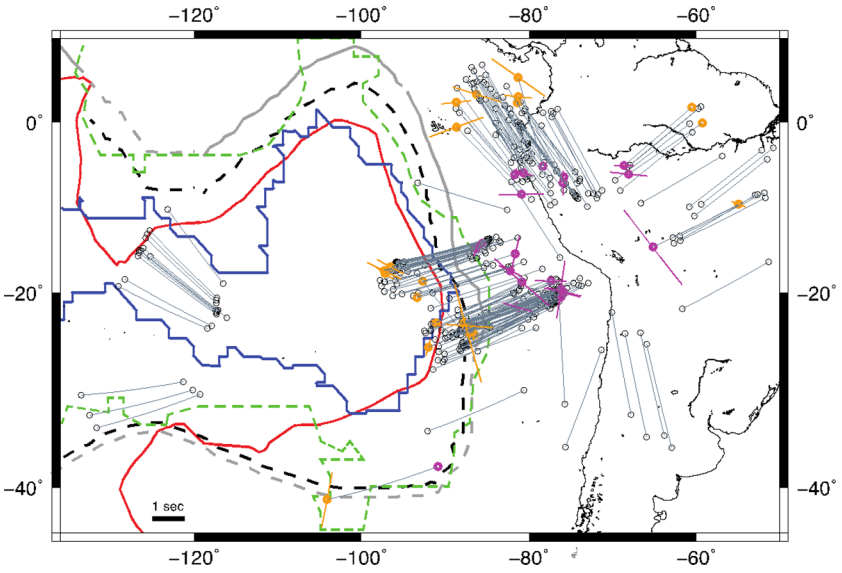

Figure 11. All SKS–SKKS pairs plotted at 2700 km pierce points, along with estimates of the LLSVP border location. Red and orange circles denote SKS and SKKS pierce points, respectively, for pairs that exhibit an SI discrepancy greater than 0.4. Pierce points for all non-discrepant pairs are shown with white circles. Thin lines connect SKS–SKKS pairs. The orientation and length of bars correspond to measured fast directions and delay times, respectively; only splitting of discrepant pairs is shown. The red curve is the contour of $dVs = -1$ per cent based on the GyPSuM tomography model (Simmons *et al.* 2010). Two possible boundaries of the Pacific LLSVP determined with *S*-wave traveltimes residuals are also shown (grey and black contours, He & Wen 2012). The blue and green dashed curves encompass regions of consensus vote and majority vote, respectively, for the slow regions, based on a cluster analysis of global mantle tomography models (Cottaar & Lekic 2016). The black contour marks the geographic LLSVP boundary determined from the velocity perturbations and detailed waveform modeling. The grey contour is derived using the transitional boundary from positive traveltime residuals to negative or zero traveltime residuals. The dashed portion of contours indicates larger uncertainties.

mantle anisotropy likely depends on azimuth (e.g. Nowacki *et al.* 2011; Ford *et al.* 2015), while our data set suffers from poor azimuthal coverage. Furthermore, it is possible that in Regions II–IV, there is a contribution to splitting from lowermost mantle anisotropy, but both SKS and SKKS phases are split in a similar way; in this case, our SKS–SKKS splitting discrepancy technique would not be sensitive to this contribution. Another possibility is that there is lowermost anisotropy within Regions II–IV, but the anisotropic structure varies on such short length scales that stacking within the region obscures the lowermost mantle contribution. Finally, we note that because SK(K)S ray paths in the D″ layer are shorter than the ScS ray paths that are commonly used to detect lowermost mantle anisotropy, the SKS–SKKS splitting discrepancy is not sensitive to weak anisotropy (e.g. Nowacki *et al.* 2011); therefore, anisotropy may be present but undetectable if the associated SK(K)S SIs are beneath our detection limit (∼0.2 s).

4 RELATIONSHIP BETWEEN ANISOTROPY AND THE LLSVP EDGES

As in previous studies (Wang & Wen 2007; Cottaar & Romanowicz 2013; Lynner & Long 2014; Ford *et al.* 2015), we carry out a comparison between the geographic pattern of inferred lowermost mantle anisotropy from our data set and the geometry of the LLSVP edge (Fig. 11). Such a comparison may help to illuminate deformation processes at the eastern edge of the Pacific LLSVP, and test the hypothesis from previous studies that deformation, and thus anisotropy, are concentrated at LLSVP edges. The location of the eastern edge of the Pacific LLSVP is imperfectly known, but can be inferred based on seismic tomography models (Lekic *et al.* 2012; Cottaar & Lekic 2016) or on waveform modeling studies (e.g. He & Wen 2012). Specifically, He & Wen (2012) noted that the northwestern edge of the Pacific LLSVP that is rigorously resolved by waveform modeling lies inward (i.e. toward the LLSVP interior) of that constrained more loosely by traveltime analysis. This suggests that the actual eastern geographic boundary of the Pacific LLSVP may lie to the west of estimates obtained from traveltime analysis (and thus from tomographic imaging). Investigations of the eastern edge of the Pacific LLSVP from *P*-wave analysis shows that it is likely steep dipping (70°) and apparently sharp (∼40 km wide, Frost &Rost 2014), but it is not well known how similar *P*- and *S*-wave anomalies are in the lowermost mantle.

In Fig. 11, we show plausible estimates of the LLSVP edge position based on the $dVs = -1$ per cent contour of the GyPSuM tomography model (Simmons *et al.* 2010), shear wave traveltime analysis (He & Wen 2012) and recent cluster analysis on shear wave tomography models (Cottaar & Lekic 2016). We note that these different approaches generally suggest a quite consistent geographic location for the LLSVP boundary in the study area. We compare the inferred location of the boundary to our sampling of the D″ layer and find that Region I may straddle the edge of the LLSVP, with SKS phases sampling just outside it and SKKS phases sampling just within it (Fig. 11). Region II may partially intersect with the edge, while Region III likely lies entirely within it and Region IV likely lies far outside it (Fig. 11). Based on this geographic distribution and on our inference that only phases sampling Region I exhibit a contribution from lowermost mantle anisotropy, we hypothesize that strong lowermost mantle deformation capable of inducing crystallographic or shape preferred orientation (and thus anisotropy) is localized near the eastern border of the eastern LLSVP. Because Regions II, III and IV do not sample this boundary in the same way as Region I, this scenario can account for the lack of SI discrepancies in these regions.

The geographic relationship between inferred lowermost mantle anisotropy and the Pacific LLSVP documented in this study is akin to the geographic pattern inferred near the African LLSVP (Wang

& Wen 2007; Cottaar & Romanowicz 2013; Lynner & Long 2014; Ford *et al.* 2015) and the smaller scale Perm Anomaly (Long & Lynner 2015). The inferred concentration of deformation and anisotropy at the edges of LSVPs at the base of the mantle may reflect a range of processes, possibly including focused upwelling flow near the LLSVP edge at the base of a mantle plume (e.g. Steinberger & Torsvik 2012; Ford *et al.* 2015) or flow deflected or modified by the LLSVP itself (e.g. Cottaar & Romanowicz 2013; Ford *et al.* 2015). The details of this mantle flow pattern remain poorly understood, mostly due to observational difficulties in constraining the anisotropic geometry as well as experimental and modeling uncertainties in the dominant slip systems in the relevant minerals (e.g. Yamazaki *et al.* 2006; Merkel *et al.* 2007; Miyagi *et al.* 2010; Goryaeva *et al.* 2016). Despite these uncertainties, however, the observation of strong lowermost mantle anisotropy at the edges of LSVPs may provide important constraints on their formation and evolution, as well as the manner in which they interact with ambient mantle flow.

While our differential SI measurement method has some distinct strength, one disadvantage is that it cannot be used to tightly constrain the actual geometry of anisotropy. Thus, any interpretation of our results in terms of a plausible anisotropic geometry is limited by the method itself (as well as by the poor azimuthal coverage available in our study area). Despite this limitation, however, it is possible to offer a plausible geodynamic scenario based on previous studies, although we stress that our observations cannot *uniquely* constrain the geometry of anisotropy. Ford *et al.* (2015) carried out detailed forward modeling of a set of measurements of splitting due to lowermost mantle anisotropy just outside the edge of the African LLSVP, beneath the Afar region of Africa. This study found that crystallographic preferred orientation (CPO) of post-perovskite with a [100] axis that is nearly vertical or oblique to the horizontal plane provides a good fit to the observations. This model is consistent with strong anisotropy due to vertically deflected flow just outside the LLSVP edge, or with upwelling at the base of the putative Afar plume. The anisotropic model proposed by Ford *et al.* (2015) would predict splitting of SK(K)S phases that sample just outside the LLSVP boundary, with little or no splitting of phases that sample just inside the boundary; this prediction is generally consistent with our observations at the edge of the Pacific LLSVP. It may be possible to constrain the geometry of lowermost mantle anisotropy more tightly in our study region in the future by incorporating constraints on radial anisotropy from global models (e.g. Panning & Romanowicz 2006) or by making additional observations using different body wave phases. For now, however, we suggest that the anisotropy scenario proposed by Ford *et al.* (2015) for the African LLSVP edge, which invokes CPO of post-perovskite due to mantle flow with a substantial vertical component, is generally consistent with our observations.

5 CONCLUSIONS

We examined the shear wave splitting of 215 SKS–SKKS pairs measured at stations in South America and the eastern Pacific that sample a region of the lowermost mantle beneath the southeastern Pacific Ocean, in the vicinity of the eastern edge of the Pacific LLSVP. We find evidence for substantial discrepancies (greater than 0.4) in a minority (∼10 per cent) of our SKS–SKKS pairs, suggesting at least some contribution to splitting due to anisotropy in the lowermost mantle. Because our individual SKS–SKKS discrepancy observations are scattered, we introduce a waveform stacking approach to robustly identify potential contributions from D″ anisotropy. We subdivide our data set into four subregions: Region I, which likely crosses the eastern edge of the LLSVP, Region II, which partially intersects the edge, Region III, which lies entirely within the LLSVP and Region IV, which samples far outside the LLSVP. Measurements of SI values for stacked residual waveforms of SKS–SKKS pairs for each region reveal evidence for substantial splitting due to lowermost mantle anisotropy only for Region I, with weak or negligible lowermost mantle contributions from the other three regions. This can be explained by the different geographic relationships between the four regions and the edge of Pacific LLSVP. Our measurements are consistent with a scenario in which strong anisotropy is concentrated near the boundary of the Pacific LLSVP, consistent with previous findings for the African LLSVP and the Perm Anomaly. While our measurements do not tightly constrain the actual geometry of this anisotropy, the hypothesis that LLSVP edges are associated with strong anisotropy in the D″ layer is borne out by our data set, and this association may provide clues to the processes that form and maintain LLSVPs over geological time, as well as to the dynamic interaction between LLSVPs and ambient mantle convection.

ACKNOWLEDGEMENTS

Seismic data from the Global Seismograph Network (II), Global Telemetered Seismograph Network (GT), Chilean National Seismic Network (C) and Red Sismologica Nacional (CI) were used in this study, in addition to data from the Peru Lithosphere and Slab Experiment (PULSE) and the Central Andean Uplift and Geodynamics of High Topography (CAUGHT) projects. All data were accessed via the Data Management Center (DMC) of the Incorporated Research Institutions for Seismology (IRIS). We thank the IRIS PASSCAL Instrument Center as well as the many field volunteers for their support of the PULSE and CAUGHT projects. This work was supported by the National Science Foundation (NSF) via grant EAR-1550722 (MDL). The PULSE experiment was supported by NSF grants EAR-0944184 (LSW), EAR-0943991 (SLB) and EAR-0943962 (MDL). The CAUGHT experiment was supported by NSF grants EAR-0908777 (LSW) and EAR-0907880 (SLB and GZ). Some figures were prepared using the Generic Mapping Tools (Wessel and Smith 1991). We are grateful to two anonymous reviewers for thoughtful and constructive suggestions that improved the paper.

REFERENCES

Antonijevic, S.K., Wagner, L.S., Beck, S.L., Long, M.D., Zandt, G. & Tavera, H., 2016. Effects of change in slab geometry on the mantle flow and slab fabric in Southern Peru, *J. geophys. Res.*, **121**, doi:2016JB013064.

Chevrot, S., 2000. Multichannel analysis of shear wave splitting, *J. geophys. Res.*, **105**, 21579–21590.

Cottaar, S. & Lekic, V., 2016. Morphology of seismically slow lower-mantle structures, *Geophys. J. Int.*, **207**, 1122–1136.

Cottaar, S. & Romanowicz, B., 2013. Observations of changing anisotropy across the southern margin of the African LLSVP, *Geophys. J. Int.*, **195**, 1184–1195.

Crotwell, H.P., Owens, T.J. & Ritsema, J., 1999. The TauP Toolkit: flexible Seismic travel-time and ray-path utilities, *Seismol. Res. Lett.*, **70**, 154–160.

Eakin, C.M. & Long, M.D., 2013. Complex anisotropy beneath the Peruvian flat slab from frequency-dependent, multiple-phase shear wave splitting analysis, *J. geophys. Res.*, **118**, 4794–4813.

Eakin, C.M., Long, M.D., Beck, S.L., Wagner, L.S., Tavera, H. & Condori, C., 2014. Response of the mantle to flat slab evolution: insights from local S splitting beneath Peru, *Geophys. Res. Lett.*, **41**, 3438–3446.

Eakin, C.M., Long, M.D., Wagner, L.S., Beck, S.L. & Tavera, H., 2015. Upper mantle anisotropy beneath Peru from SKS splitting: constraints on flat slab dynamics and interaction with the Nazca Ridge, *Earth planet. Sci. Lett.*, **412**, 152–162.

Ford, H.A., Long, M.D., He, X. & Lynner, C., 2015. Lowermost mantle flow at the eastern edge of the African Large Low Shear Velocity Province, *Earth planet. Sci. Lett.*, **420**, 12–22.

Frost, D.A. & Rost, S., 2014. The P-wave boundary of the Large-Low Shear Velocity Province beneath the Pacific, *Earth planet. Sci. Lett.*, **403**, 380–392.

Garnero, E.J., McNamara, A.K. & Shim, S.H., 2016. Continent-sized anomalous zones with low seismic velocity at the base of Earth's mantle, *Nat Geosci,*, **9**, 481–489.

Garnero, E.J., Moore, M.M., Lay, T. & Fouch, M.J., 2004. Isotropy or weak vertical transverse isotropy in D″ beneath the Atlantic Ocean, *J. geophys. Res.*, **109**, B08308, doi: 10.1029/2004JB003004.

Goryaeva, A.M., Carrez, P. & Cordier, P., 2016. Low viscosity and high attenuation in MgSiO3 post-perovskite inferred from atomic-scale calculations, *Sci. Rep.*, **6**, 34771, doi:10.1038/srep34771.

He, X. & Long, M.D., 2011. Lowermost mantle anisotropy beneath the northwestern Pacific: evidence from PcS, ScS, SKS, and SKKS phases, *Geochem. Geophys. Geosyst.***12**, Q12012, doi:10.1029/2011GC003779.

He, Y. & Wen, L., 2012. Geographic boundary of the "Pacific Anomaly" and its geometry and transitional structure in the north, *J. geophys. Res.*, **117**, B09308, doi:10.1029/2012JB009436.

Lay, T. & Garnero, E.J., 2004. Core-mantle boundary structures and processes, in *State of the Planet: Frontiers and Challenges in Geophysics*, Vol. **150**, pp. 25–41, eds Sparks, R.S.J. & Hawkesworth, C.J., AGU, Washington, DC.

Lay, T. & Helmberger, D.V., 1983. The shear-wave velocity-gradient at the base of the mantle, *J. geophys. Res.*, **88**, 8160–8170.

Lay, T., Hernlund, J., Garnero, E.J. & Thorne, M.S., 2006. A post-perovskite lens and D″ heat flux beneath the Central Pacific, *Science*, **314**, 1272–1276.

Lekic, V., Cottaar, S., Dziewonski, A. & Romanowicz, B., 2012. Cluster analysis of global lower mantle tomography: a new class of structure and implications for chemical heterogeneity, *Earth planet. Sci. Lett.*, **357**, 68–77.

Lin, Y.P., Zhao, L. & Hung, S.H., 2014. Full-wave effects on shear wave splitting, *Geophys. Res. Lett.*, **41**, 799–804.

Long, M.D., 2009. Complex anisotropy in D″ beneath the eastern Pacific from SKS–SKKS splitting discrepancies, *Earth planet. Sci. Lett.*, **283**, 181–189.

Long, M.D., Biryol, C.B., Eakin, C.M., Beck, S.L., Wagner, L.S., Zandt, G., Minaya, E. & Tavera, H., 2016. Overriding plate, mantle wedge, slab, and subslab contributions to seismic anisotropy beneath the northern Central Andean Plateau, *Geochem. Geophys. Geosyst.*, **17**, 2556–2575.

Long, M.D., Gao, H.Y., Klaus, A., Wagner, L.S., Fouch, M.J., James, D.E. & Humphreys, E., 2009. Shear wave splitting and the pattern of mantle flow beneath eastern Oregon, *Earth planet. Sci. Lett.*, **288**, 359–369.

Long, M.D. & Lynner, C., 2015. Seismic anisotropy in the lowermost mantle near the Perm Anomaly, *Geophys. Res. Lett.*, **42**, doi:2015GL065506.

Lynner, C. & Long, M.D., 2012. Evaluating contributions to SK(K)S splitting from Lower Mantle Anisotropy: a case study from station DBIC, Côte D'Ivoire, *Bull. seism. Soc. Am.*, **102**, 1030–1040.

Lynner, C. & Long, M.D., 2014. Lowermost mantle anisotropy and deformation along the boundary of the African LLSVP, *Geophys. Res. Lett.*, **41**, 3447–3454.

McNamara, A.K., Garnero, E.J. & Rost, S., 2010. Tracking deep mantle reservoirs with ultra-low velocity zones, *Earth planet. Sci. Lett.*, **299**, 1–9.

Meade, C., Silver, P.G. & Kaneshima, S., 1995. Laboratory and seismological observations of lower mantle isotropy, *Geophys. Res. Lett.*, **22**, 1293–1296.

Merkel, S., McNamara, A.K., Kubo, A., Speziale, S., Miyagi, L., Meng, Y., Duffy, T.S. & Wenk, H.-R., 2007. Deformation of (Mg,Fe)SiO3 post-perovskite and D″ anisotropy, *Science*, **316**, 1729–1732.

Miyagi, L., Kanitpanyacharoen, W., Kaercher, P., Lee, K.K.M. & Wenk, H.-R., 2010. Slip systems in MgSiO3 post-perovskite: implications for D″ anisotropy, *Science*, **329**, 1639–1641.

Murakami, M., Hirose, K., Kawamura, K., Sata, N. & Ohishi, Y., 2004. Post-perovskite phase transition in MgSiO3, *Science*, **304**, 855–858.

Niu, F.L. & Perez, A.M., 2004. Seismic anisotropy in the lower mantle: a comparison of waveform splitting of SKS and SKKS, *Geophys. Res. Lett.*, **31**, doi:10.1029/2004GL021196.

Nowacki, A., Wookey, J. & Kendall, J.M., 2011. New advances in using seismic anisotropy, mineral physics and geodynamics to understand deformation in the lowermost mantle, *J. Geodyn.*, **52**, 205–228.

Panning, M. & Romanowicz, B., 2006. A three-dimensional radially anisotropic model of shear velocity in the whole mantle, *Geophys. J. Int.*, **167**, 361–379.

Restivo, A. & Helffrich, G., 2006. Core-mantle boundary structure investigated using SKS and SKKS polarization anomalies, *Geophys. J. Int.*, **165**, 288–302.

Rost, S., Garnero, E.J., Williams, Q. & Manga, M., 2005. Seismological constraints on a possible plume root at the core-mantle boundary, *Nature*, **435**, 666–669.

Shearer, P.M., 1991. Constraints on upper mantle discontinuities from observations of long-period reflected and converted phases, *J. geophys. Res.*, **96**, 18147–18182.

Sidorin, I., Gurnis, M. & Helmberger, D.V., 1999. Evidence for a ubiquitous seismic discontinuity at the base of the mantle, *Science*, **286**, 1326–1331.

Silver, P.G. & Long, M.D., 2011. The non-commutivity of shear wave splitting operators at low frequencies and implications for anisotropy tomography, *Geophys. J. Int.*, **184**, 1415–1427.

Simmons, N.A., Forte, A.M., Boschi, L. & Grand, S.P., 2010. GyPSuM: a joint tomographic model of mantle density and seismic wave speeds, *J. geophys. Res.*, **115**, B12310, doi:10.1029/2010JB007631.

Steinberger, B. & Torsvik, T.H., 2012. A geodynamic model of plumes from the margins of Large Low Shear Velocity Provinces, *Geochem. Geophys. Geosyst.*, **13**, doi:2011GC003808.

Trampert, J., Deschamps, F., Resovsky, J. & Yuen, D., 2004. Probabilistic tomography maps chemical heterogeneities throughout the lower mantle, *Science*, **306**, 853–856.

Vanacore, E. & Niu, F.L., 2011. Characterization of the D″ beneath the Galapagos Islands using SKKS and SKS waveforms, *Earthq. Sci.*, **24**, 87–99.

Wang, Y. & Wen, L.X., 2007. Complex seismic anisotropy at the border of a very low velocity province at the base of the Earth's mantle, *J. geophys. Res.*, **112**, B09305, doi:10.1029/2006JB004483.

Wessel, P. & Smith, W.H.F., 1991. Free software helps map and display data, *EOS, Trans. Am. Geophys. Un.*, **72**, 441–446.

Wolfe, C.J. & Silver, P.G., 1998. Seismic anisotropy of oceanic upper mantle: shear wave splitting methodologies and observations, *J. geophys. Res.*, **103**, 749–771.

Wookey, J. & Kendall, J.M., 2007. Seismic anisotropy of post-perovskite and the lowermost mantle, *Geophys. Monogr. Ser.*, **174**, 171–189.

Wüstefeld, A., Bokelmann, G., Zaroli, C. & Barruol, G., 2008. SplitLab: a shear-wave splitting environment in Matlab, *Comp. Geosci.*, **34**, 515–528.

Yamazaki, D., Yoshino, T., Ohfuji, H., Ando, J.I. & Yoneda, A., 2006. Origin of seismic anisotropy in the D″ layer inferred from shear deformation experiments on post-perovskite phase, *Earth planet. Sci. Lett.*, **252**, 372–378.

SUPPORTING INFORMATION

Supplementary data are available at *GJI* online.

Table S1. All of the observations used in this study along with their corresponding splitting intensity measurements.

Please note: Oxford University Press is not responsible for the content or functionality of any supporting materials supplied by the authors. Any queries (other than missing material) should be directed to the corresponding author for the paper.